npj | biomedical innovations

Article

https://doi.org/10.1038/s44385-025-00017-x

VITALS: an implantable sensor network for postoperative cardiac monitoring in heart failure patients

Check for updates

Ali Kight[1] ✉, Moussa Haidar[2], Masafumi Shibata[2], Yoshikazu Ono[2], Gentaro Ikeda[3], Amit Sharir[2], Federica Semproni[4], Yellappa Palagani[2], Sawson Taheri[5], Amy Kyungwon Han[6], Michael Ma[2], Kirk Riemer[2], Doff B. McElhinney[3,7], Seraina A. Dual[8] & Mark Cutkosky[9]

Heart Failure (HF) is a global epidemic, with high readmission rates and significant morbidity persisting due to gaps in post-acute care.Traditional follow-up often misses gradual postoperative cardiac deterioration occurring outside hospital settings. While advances in remote patient monitoring show promise, practical, continuous, and sensitive methods remain lacking. Building on previous work introducing a durable, soft strain sensor, this research presents VITALS, an implantable strain sensing network that enables continuous biventricular, multiaxial monitoring of cardiac function. The sensor's design demonstrates improved fatigue life in bechtop testing compared to other soft, large-deformation strain sensors, while effectively minimizing shear loading effects to enhance accuracy. Additionally, the network integrates a sensor on the aorta for synchronous systolic pressure monitoring. Acute animal studies demonstrate the potential of VITALS' to track epicardial strain, detect preload changes rapidly, and differentiate inotropic states. Validation against echocardiographic chamber volumes and GLS provides preliminary support of the sensor's clinical relevance.

Heart Failure (HF) is a significant health burden, affecting over 6 million adults in the US and costing upwards of $30B annually[1]. Advanced cardiovascular interventions, including surgical procedures and implantation of mechanical circulatory support devices, are continually improving and significantly impacting HF patient health and lifespans. Despite these advancements, a critical gap in post-acute care persists, as evidenced by the persistently high unplanned readmission rates of up to 20%[2,3]. HF patients face a significantly higher postoperative mortality risk across various surgical settings compared to those without HF[4]. This risk is particularly pronounced in complex surgeries, where the one-year mortality rate can reach up to 30%, underscoring a crucial need for improved care for these high-risk patients[5].

The postoperative deterioration of cardiac function, which can develop over the course of days or weeks, typically occurs outside of the hospital setting and cannot be adequately captured by the intermittent nature of follow-up assessments in clinic[6]. By the time a patient's symptoms manifest, further irreversible myocardial changes and functional impairment may have occurred[7–12]. Without the ability to tightly monitor patients, a cycle of worsening conditions emerges: hospitalization, treatment, deterioration, readmission, and so on[13,14].

Early detection of worsening cardiac function in both left ventricle (LV) and right ventricle (RV) is imperative for effective post-acute care of high-risk HF patients[10,15–17]. Recent studies have underscored the significance of measuring myocardial deformation, particularly strain, as a robust early indicator of cardiac dysfunction[18–20]. Recent preclinical investigations offer compelling evidence that abnormalities in myocardial strain manifest much earlier than other defining factors, such as ventricular filling pressures, in the progression of heart failure, and support strain's superior sensitivity and prognostic value compared to global metrics of direct cardiac function, such as ejection fraction (EF)[21–27]. Strain is a spatially specific metric that can be acquired across multiple axes, with a demonstrated ability to offer incremental prognostic insights. The axis-specific strain and their interrelationships enable pathophysiological phenotyping for improved disease stratification[28,29]. Additionally, studies have demonstrated that left

[1]Department of Bioengineering, Stanford University, Stanford, USA. [2]Department of Cardiothoracic Surgery, Pediatric Cardiac Surgery Division, Stanford School of Medicine, Palo Alto, USA. [3]Clinical and Translational Research Program, Lucile Packard Children's Hospital, Stanford University, Stanford, USA. [4]BioRobotics Institute, Scuola Superiore Sant'Anna, Pisa, Italy. [5]Department of Electrical Engineering, Stanford University, Stanford, USA. [6]Department of Mechanical Engineering, Seoul National University, Gwanak-gu, South Korea. [7]Department of Cardiothoracic Surgery, Lucile Packard, Children's Hospital, Stanford University, Stanford, USA. [8]Department of Biomedical Engineering and Health Systems, KTH Royal Institute of Technology, Stockholm, Sweden. [9]Department of Mechanical Engineering, Stanford University, Stanford, USA. ✉e-mail: akight@stanford.edu

ventricular epicardial strain correlates well with preload and stroke volume, highlighting its utility in evaluating hemodynamic parameters[30]. Moreover, strain measurements can extend beyond cardiac tissue; for instance, measuring circumferential strain on compliant outflow vessels like the aorta can aid in estimating systolic pressure[31]. In summary, these attributes position strain as a potent tool for patient stratification and guiding condition-specific clinical decisions.

However, conventional methods for assessing strain, such as speckle tracking echocardiography, have limitations in providing continuous monitoring and may not be practical for remote use, hindering their ability to capture early signals of dysfunction that typically occur at home[30,32]. Recent advancements in wearable and implantable sensing technologies offer promise in bridging the gap in care for HF patients, enabling timely interventions to reduce unplanned hospital readmissions and improve patient outcomes[33]. Thus, enabling continuous measurements of strain through an implantable monitoring system could address current clinical limitations, offering a comprehensive assessment of cardiac function crucial for guiding clinical decision-making and improving outcomes in high-risk, postoperative HF patients.

In this study, we investigate the feasibility and utility of continuous, direct measurements of strain for functional cardiac monitoring. We propose employing a large deformation soft sensor that decouples mechanical transmission and electrical transduction, a method demonstrated to enhance durability without compromising soft mechanical properties[34], and present encapsulation techniques to mitigate the effects of non-axial loading conditions and changing boundary conditions on sensor signals. This solution would be non-blood contacting and implanted onto the epicardium adjunctively during advanced surgical procedures in high-risk patients, and offer continuous remote monitoring of heart function to facilitate proactive, patient-specific therapeutic titration or surgical intervention. The design considers the challenges associated with such a demanding application, showcasing design principles that are well-suited for engineering optimization necessary for full implantability, allowing for the choice of biocompatible materials and waterproof coatings as well as compatibility with standard wireless communication methods.

To assess the clinical relevance of our approach, we developed a prototype of an implantable, epicardial sensing network named VITALS (Versatile Implant for Telemetry And Longitudinal Sensing). With this prototype, we demonstrate the advantages of patterning the sensor in a multi-axial configuration and integrating synchronous aortic strain measurement. We evaluate the sensor network's performance under various conditions in vivo (Fig. 1C). Through a series of large animal experiments, we demonstrate initial feasibility of this sensor network, showing correlation with gold-standard clinical metrics in a controlled, acute setting. Our preliminary results suggest potential for providing continuous insights into cardiac hemodynamics, function, and inotropic state. This validation is a crucial first step towards dynamic monitoring of the heart.

Results

Sensing technology

A durable, modular sensing paradigm for non-blood-contacting strain monitoring of cardiac and vascular tissue. Significant research efforts have been dedicated to developing biocompatible strain sensors that match the compliance of soft biological tissues. However, these technologies have often failed to translate to the clinic due to limitations in durability and robustness over time[35–37]. The heart, as a highly dynamic organ responsible for continuous oxygenation, undergoes over 1 million cycles in just two weeks. This extreme mechanical demand requires sensor materials to either be inherently biocompatible or encapsulated with biocompatible coatings, which further restricts the design options for these sensors. Central to this challenge is achieving a balance between high mechanical compliance and the electrical integrity of the conductive sensing structures. This balance is particularly difficult due to the contrasting demands for soft mechanical properties and reliable, sustained electrical performance[38]. Several research groups have attempted to address this problem through two primary approaches, each with its own limitations.

The first approach involves doping elastomers with conductive materials to provide electrical conductivity, enabling strain sensing through changes in resistance. While this method can produce materials capable of withstanding large deformations, it frequently leads to signal drift after only a few thousand loading cycles[37,39,40]. This drift compromises the sensor's ability to accurately measure strain over extended periods, especially in applications requiring long-term monitoring under physiologically dynamic conditions. In some cases, switching to capacitive or inductive sensing has been proposed to reduce drift; however, issues with packaging and maintaining electrical integrity remain a challenge[41].

The second approach involves using highly conductive materials, such as metals or graphene, configured into complex geometric patterns, like serpentine structures, that accommodate stretchability[42]. While these designs can be optimized to enable multi-directional deformation and reduce stress concentrations through encapsulation strategies, incorporating rigid materials into a cardiac sensing system introduces additional challenges. Specifically, such designs increase the risk of delamination between rigid elements and the encapsulant, particularly in the heart's highly dynamic environment, which undergoes millions of strain cycles. These complexities add multiple potential points of failure, increasing the overall risk and limiting long-term reliability. Consequently, minimizing the use of rigid, non-stretchable materials is ideal for cardiac applications to simplify design and enhance durability in this demanding environment.

In response to these challenges, the authors previously developed a uniaxial strain-sensing mechanism that separates substrate deformation from the electrical transduction mechanism through a mechanical transmission[34]. This approach leverages a non-conductive, soft transmission element coupled to a high-sensitivity micro-electromechanical system (MEMS) sensor, allowing mechanical energy from high-strain deformations to be reliably converted into electrical signals (Fig. 1D). Specifically, a MEMS barometric pressure sensor is integrated with a soft silicone element, which deforms in response to strain. As the silicone stretches, the pressure detected by the MEMS sensor decreases proportionally to the strain experienced by the silicone. This design enables the development of a strain sensor with a stiffness comparable to that of cardiac tissue, capable of undergoing over one million cycles without measurable drift or degradation when assessed in a benchtop setting[34].

A comparison of this sensor with other strain sensors reported in the literature, with respect to demonstrated cycle life and mechanical properties, is displayed in Fig. 1E. Although the demonstrated one million cycles translates to approximately two weeks of continuous cardiac motion, this represents a conservative lower bound rather than a failure point. Mechanical durability testing was performed using a muscle lever (300C Dual Mode Muscle Lever, Aurora Scientific) under physiological strain levels (20% peak strain) and frequencies (1.5 Hz). For a more detailed quantitative analysis and model on hysteresis compensation, interested readers are referred to the author's previous publication[34]. Throughout testing, sensors maintained consistent sensitivity with no observable drift, delamination, or mechanical degradation. This robustness is consistent with established research on silicone rubber fatigue, which demonstrates predictable and reliable performance under cyclic loading within material strain limits[43–45]. The sensor design operates within favorable regimes for key fatigue factors including strain magnitude, loading rate, and temperature, suggesting potential for sustained operation well beyond the tested cycles—although future studies will include longer cycling times under relevant physiological conditions. Additionally, the sensor exhibits relative insensitivity to off-axis deformations, such as bending, due to the low stiffness of the silicone element. Corroborating the empirical findings in[34], a finite element analysis of the sensor's response to non-axial loading is presented in the Supplementary Material, Supplementary Fig. 6. Moreover, the MEMS barometers selected for this application (BMP384, Bosch) feature a gel-filled cavity, providing robustness against water and making them well-suited for the application. To support this assertion, results from an accelerated aging

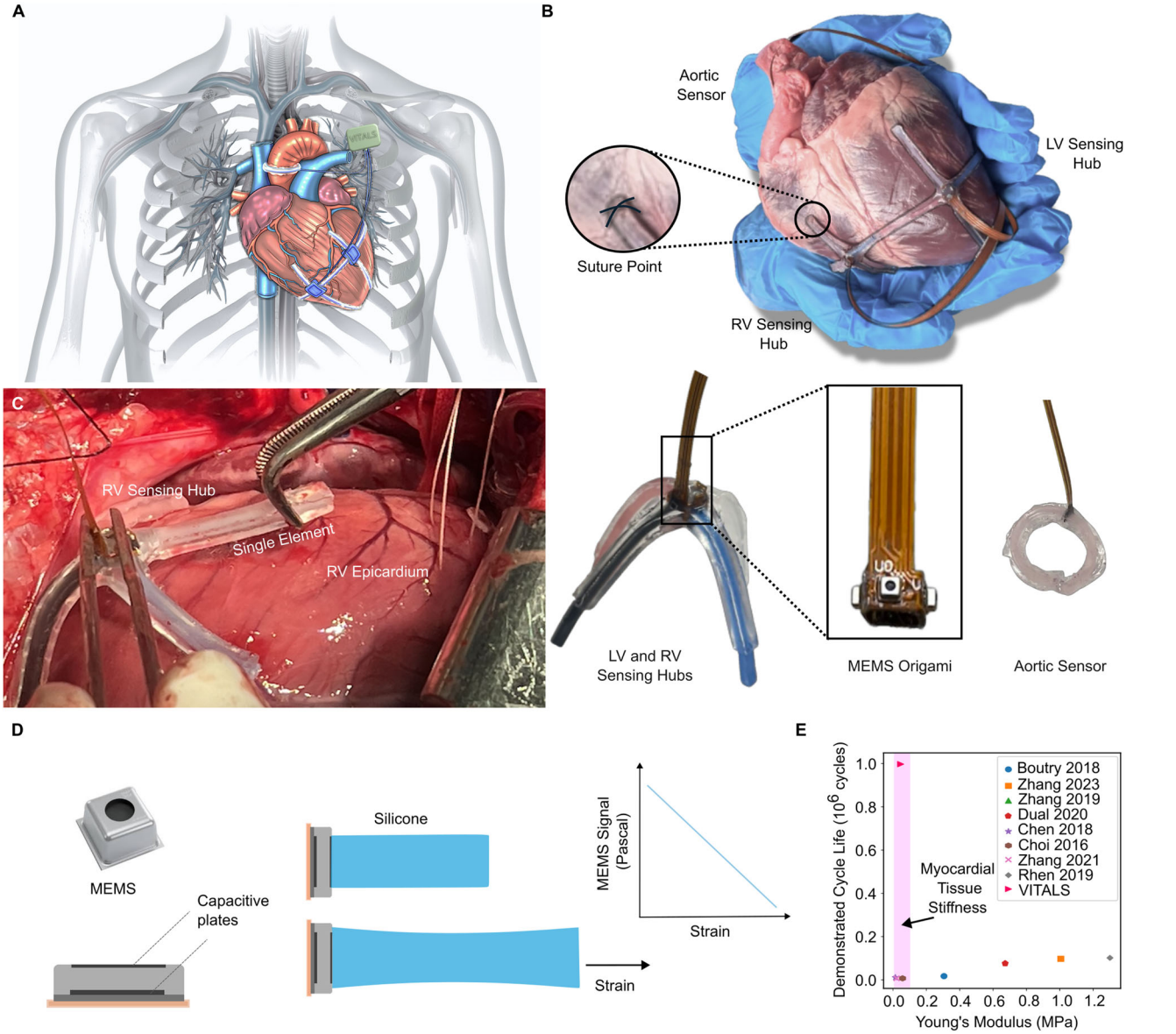


Fig. 1 | The VITALS network concept. A Illustration of the VITALS network and associated electronics implanted on a patient's epicardium, illustrating the positioning and integration of the network. **B** Visualization of the VITALS network affixed to an ex-vivo porcine heart, highlighting a typical suture point in the inset. Both the left ventricular (LV) and right ventricular (RV) sensing hubs, each comprising four sensors enabled by origami-folded circuitry, are marked. The aortic sensor, obscured by the pulmonary artery, is indicated with visible wiring. **C** Image of a single sensing hub attachment to the RV epicardium during an in vivo experiment. **D** A visualization of the sensing mechanism, whereby a capacitive microelectromechanical system (MEMS) barometric pressure sensor is coupled to a soft silicone element. When the element is stretched, sensed pressure decreases proportionally, as seen in the represenative graph. **E** A comparison of VITALS to other stretchable strain sensors reported in literature with respect to demonstrated cycle life and stiffness (References are in order of top to bottom[30,96–102]). The range for myocardial tissue stiffness is shaded in pink[103].

test in saline can be found in Supplementary Materials, Supplementary Fig. 7.

A low-stiffness encapsulant for reduced sensitivity to shear loading. To ensure reliable performance, the sensor must remain selective to the intended measurement, unaffected by external mechanical forces. Dynamic deformation of implantable structures—particularly shear forces arising from boundary condition changes such as fibrotic adhesions expected during long-term implantation or tissue interactions — can distort sensor readings, leading to inaccuracies.

To address this concern, a mechanical isolation strategy was developed using a low-stiffness silicone gel encapsulation to reduce sensitivity to shear forces. A 1 mm layer of Ecoflex™ 000-35 silicone gel is cast around the sensor, creating a buffer that dissipates shear forces, preventing them from reaching the internal sensing element, as shown in Fig. 2A. The sensor itself is made from Ecoflex™ 00-10, which is four times stiffer than the gel, ensuring that deformation occurs primarily in the gel, thus preserving measurement accuracy. The Ecoflex material was selected for construction to prioritize both mechanical performance and biocompatibility[46]. Ecoflex™ silicones have a documented history of use in medical devices and implant research due to their biocompatibility and stable mechanical properties. Previous work by our group with similar epicardial devices using these materials demonstrated good biocompatibility in small animal models, showing negligible inflammation[47].

A benchtop study evaluated the effectiveness of this multimaterial encapsulation on a prolate-spheroidal ventricular phantom, designed to

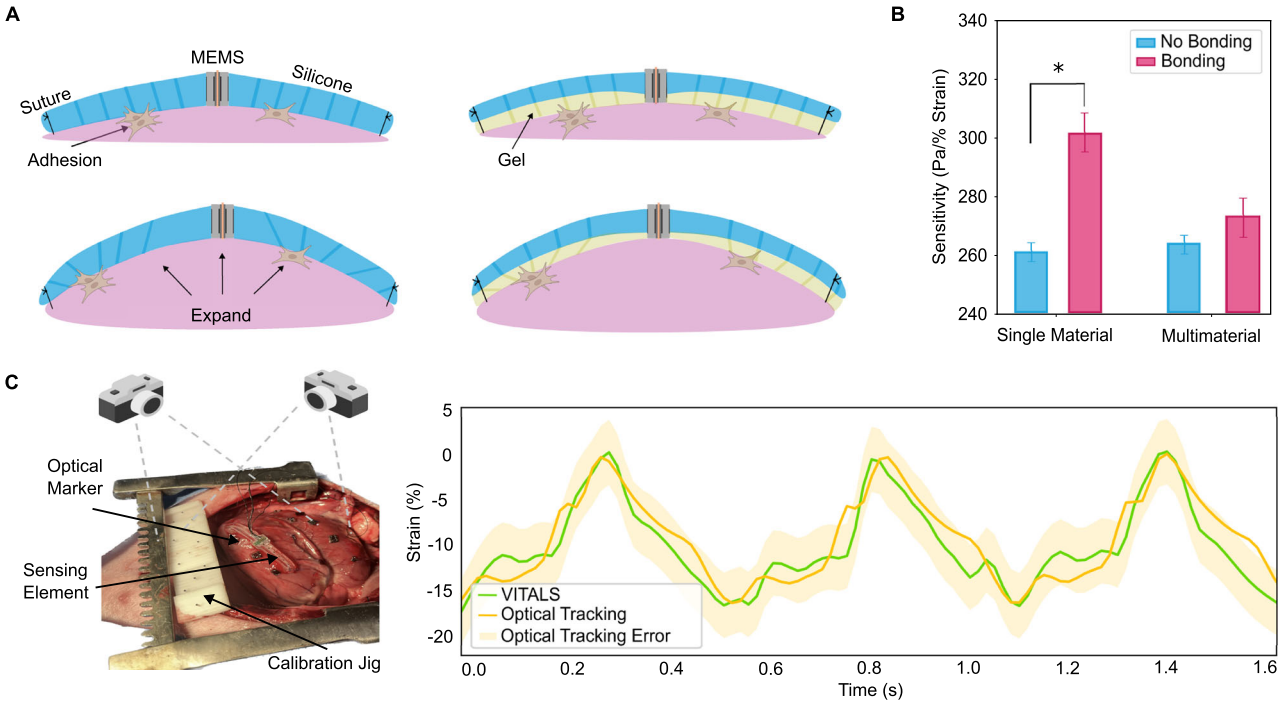


Fig. 2 | Validation of the multimaterial strategy in benchtop and in vivo sensor accuracy. A (Left) A single-material sensor with modified boundary conditions due to tissue adhesion, resulting in a complex deformation pattern along its length during stretch. (Right) The integration of a soft gel layer absorbs the load through shear strain, allowing the sensing element to deform uniformly. **B** Benchtop experiment using a ventricular phantom illustrating the impact of the gel on the sensor's signal. A sensor modeled after the left illustration in **A**, made of Ecoflex™ 00-10 silicone (single material), was compared with a sensor from the right illustration in **A**, where the sensing element is made of Ecoflex™ 00-10 with a coating of Ecoflex™ 000-35 gel (multimaterial). To simulate adhesion, the sensor was bonded to the phantom's surface using cyanoacrylate, and the signal amplitude was recorded during inflation. The single-material sensor showed a statistically significant change in signal (p-value = 0.0013), while the multimaterial sensor showed no significant difference (p-value = 0.099). **C** Image of the in vivo setup comparing sensor accuracy using stereophotogrammetry and optical markers on epicardial tissue. The sensor strain had a root mean square error of 2.2% strain, or 0.56 mm, compared to the optically tracked strain reference.

simulate myocardial tissue. Shear loading was simulated by bonding the sensor to the phantom at a discrete point using cyanoacrylate. The study compared single-material and multimaterial sensors, with and without shear loading, over three inflation cycles. In Fig. 2B, the sensitivity of single material and multimaterial sensors is shown under bonded and non-bonded conditions. The nominal sensitivity of the single material sensor without bonding is approximately 261 Pa per % strain, which is sufficiently high given the MEMS barometer's unfiltered RMS noise of 1.2 Pa and a relative accuracy of 9 Pa (BMP384, Bosch). With multimaterial fabrication, the sensitivity remains approximately 264 Pa per % strain, indicating negligible change of 1.1% in sensitivity with the addition of the gel. When comparing bonded and unbonded scenarios, the single material sensor exhibited a 15.7% change in strain signal under shear loading, whereas the multimaterial sensor showed only a 3.4% change (Fig. 2B), suggesting that the encapsulation strategy reduces sensitivity to shear forces under simulated conditions while preserving sensor accuracy.

In vivo experiments demonstrate accuracy of sensing paradigm under physiological conditions. Cardiac deformation during the cardiac cycle is an intricate process. The heart's structural dynamics involve not only contraction and relaxation but also a sophisticated pattern of twisting and untwisting, coupled with dynamically changing curvature of the ventricles. These complex movements are fundamental to the heart's pumping function, yet they present a significant challenge for accurate real-time monitoring of cardiac deformation. The design of VITALS incorporates features intended to address these challenges. By anchoring the sensor elements solely at their respective distal ends, the total change in length of each axis is captured without interference from twisting motions. Moreover, the gel encapsulation mechanically isolates the sensing element, making the signal insensitive to changes in friction that might occur due to dynamic normal forces as a function of curvature changes over contraction, a consideration raised in previous work[34].

To characterize the accuracy of the sensing paradigm, we employed an in vivo experimental set-up in an acute, open-chest porcine model ($n = 1$). A single sensing element was attached to the epicardium of the LV with two sutures, and the sensor signal was read continuously in real-time at 200Hz. Reference epicardial strain was measured using optical markers placed next to the sensor and tracked using stereophotogrammetry methods (Fig. 2C)[48]. By simultaneously tracking two points on a rigid object located within the field of view, a baseline for measurement error of the reference strain measurement was also established. As illustrated in Fig. 2C, the strain measurements obtained from the VITALS element were consistently within measurement error of the optically tracked strain, specifically demonstrating a root mean square error of 2.2% strain or 0.56 mm compared to ground-truth optical strain (%) or change in length (mm), respectively, over three cycles.

While the current sensor design prioritizes measurement of global strain metrics (GLS and GCS) through end-point attachment, local strain measurements could provide additional diagnostic value, particularly in identifying regional abnormalities such as infarcted tissue. The decision to measure global strain aligns with current clinical standards and enables direct comparison with established echocardiographic metrics. Future iterations of the device could incorporate additional sensing elements along each axis to enable more granular strain mapping, though this would need to be balanced against the increased complexity of device placement and data processing.

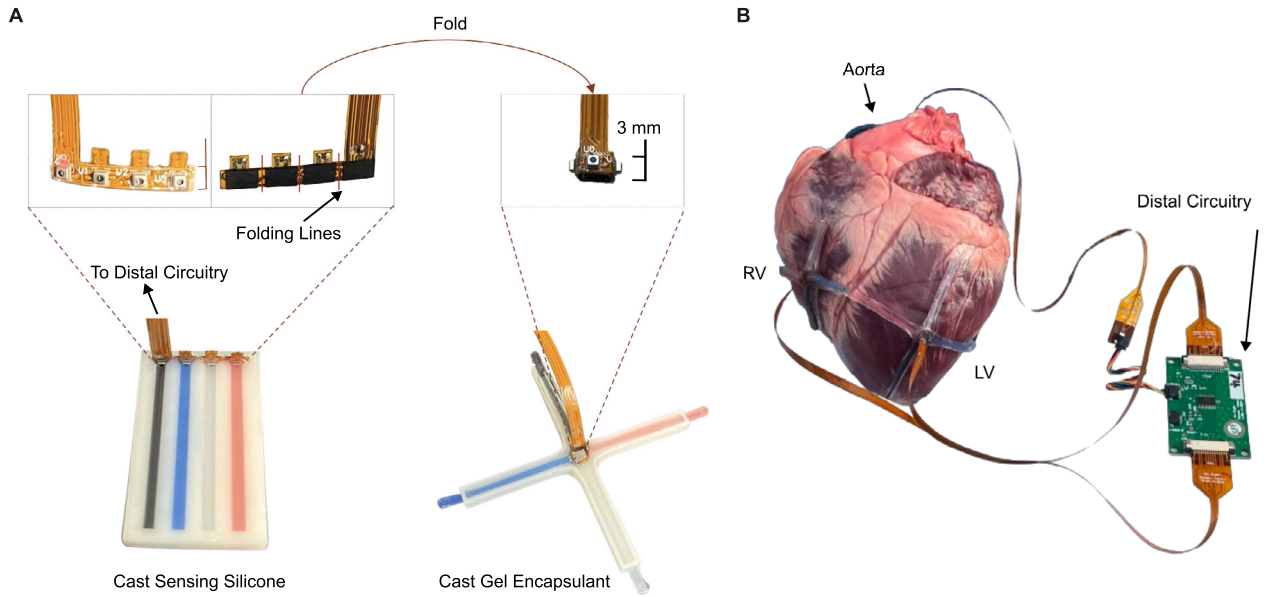


Fig. 3 | Fabrication of the sensor network. A The VITALS sensing hub is initially fabricated on a flat, flexible printed circuit board (PCB) that incorporates a selective stiffener to aid in folding. This flat PCB is placed into a 3D-printed mold, designed to create four distinct sensing elements. Following the molding process, the PCB is folded at the predetermined lines and secured in place using medical device-grade cyanoacrylate adhesive. Next, each sensing element is individually encapsulated with gel in a separate 3D-printed mold. To ensure complete encapsulation, each sensing element is suspended within the mold to form a 1 mm layer on all four sides of the sensing element. This is done by applying tension to the element and threading the end through a gap located at the extremity of each mold arm. **B** The sensor array is then integrated into a network, including both RV and LV sensing hubs and a single aortic sensor connected to a custom circuit board. This board is equipped with two I2C multiplexers, enabling communication with the nine sensors in the network. Data is relayed to a microcontroller and PC for readout. More detailed information on the high-level system and circuit design can be found in Supplementary Materials, Supplementary Figures 3 and 4.

Sensing network and in vivo experimentation

Origami folding for multiaxis, biventricular sensing. The heart's mechanical pumping efficiency can be attributed to its geometrically complex fiber architecture. The muscular layers of the heart are oriented in helical configurations, with the fiber angles varying transmurally throughout the ventricular walls. This architecture gives rise to complex three-dimensional motions in both the right and left ventricles. The axis-specific functional impairment has proven an important feature for diagnostic stratification[49]. For example, in the RV, the axis of impaired strain, longitudinal versus circumferential, can signify pressure versus volume overload in the failing heart, respectively[28]; whereas in the LV, an increase in circumferential strain with a concomitant decrease in longitudinal strain is a strong predictor of incident heart failure and mortality, even when ejection fraction (EF) is normal[29]. To impart directional strain sensitivity, and inspired by the helical structure of the native myocardium, a multiaxis sensing architecture was developed. Four MEMS barometers are mounted onto a flexible printed circuit board (PCB) strip with additional polyimide stiffeners placed behind each MEMS component (Fig. 3A). A 3D printed mold is used to cast the four elastomeric elements onto the circuit strip using Ecoflex™ 00-10 according to previous methods[34]. The cast PCB is folded along the stiffener lines to form a three-dimensional shape, as in origami, and sealed with medical-grade cyanoacrylate. The structure is then placed in a second 3D printed mold where the low stiffness encapsulating gel (Ecoflex™ Gel) is cast. The MEMS barometer signals travel via this thin, flexible cable to a distal circuitry hub. Notably, the structure is a contiguous unit, in that the flex PCB also forms the flexible cable, minimizing the risk of susceptible connection point fatigue. This design choice was inspired by the mechanically separated architecture of pacemaker leads and pulse generators, whereby the circuitry can be consolidated into a robust package and placed in the pectoral region. In this way, the soft, epicardial sensing network is less affected by mechanical influence, such as torque or strain, from the circuitry. A detailed illustration of the circuit can be found in the Supplementary Materials, Supplementary Fig. 3.

The sensor network. Two sensing hubs are created using the process described above, one each for the LV and the RV. A single sensing element is also fabricated to measure aortic circumferential strain[50]. Specifically, the single sensing element is wrapped around the ascending aorta and the element's ends are sutured together, putting the sensor in slight tension to ensure stability on the vessel. More information about the aortic sensor fabrication process can be found in Supplementary Materials, Supplementary Fig. 5. The placement of the complete network on the heart is shown in Fig. 3B. For each ventricle, there are four multimaterial elastomeric elements radiating from the central electronic hub structure. The sensors are attached to the epicardium via a single suture at the distal tip of each element, in slight tension to ensure conformability and stable contact with the heart's surface, and opposing pairs of elements are combined to represent a single sensing axis. The sensing hubs are lightweight, each weighing approximately 2 grams, to avoid impeding the heart's motion. During implantation, one axis is placed from the apex to the base (Longitudinal Axis) and the other axis is anchored perpendicularly (Circumferential Axis).

Sensor correlation with clinical gold-standard metrics of LV function. Translatability and acceptability of the sensor network hinge on demonstrating its clinical relevance by comparing measurements to gold-standard metrics across a range of functional conditions. To this end, the sensing network was evaluated in a second in vivo porcine model ($n = 1$) under both healthy and induced ischemic disease states, with sensor readings compared to echocardiographic indices. The ischemic state was induced by mid-height ligation of the left anterior descending (LAD) coronary artery[51]. Concurrent echocardiographic snapshots and pressure tracings from indwelling LV and aortic catheters were captured. Global longitudinal strain (GLS), a key metric of LV contraction along the longitudinal axis, was obtained via echocardiographic speckle-tracking. The sensor network's GLS measurements showed strong agreement with the GLS values obtained via ultrasound, as seen in Fig. 4A, with minimal underestimation, likely due to the difference between epicardial strain

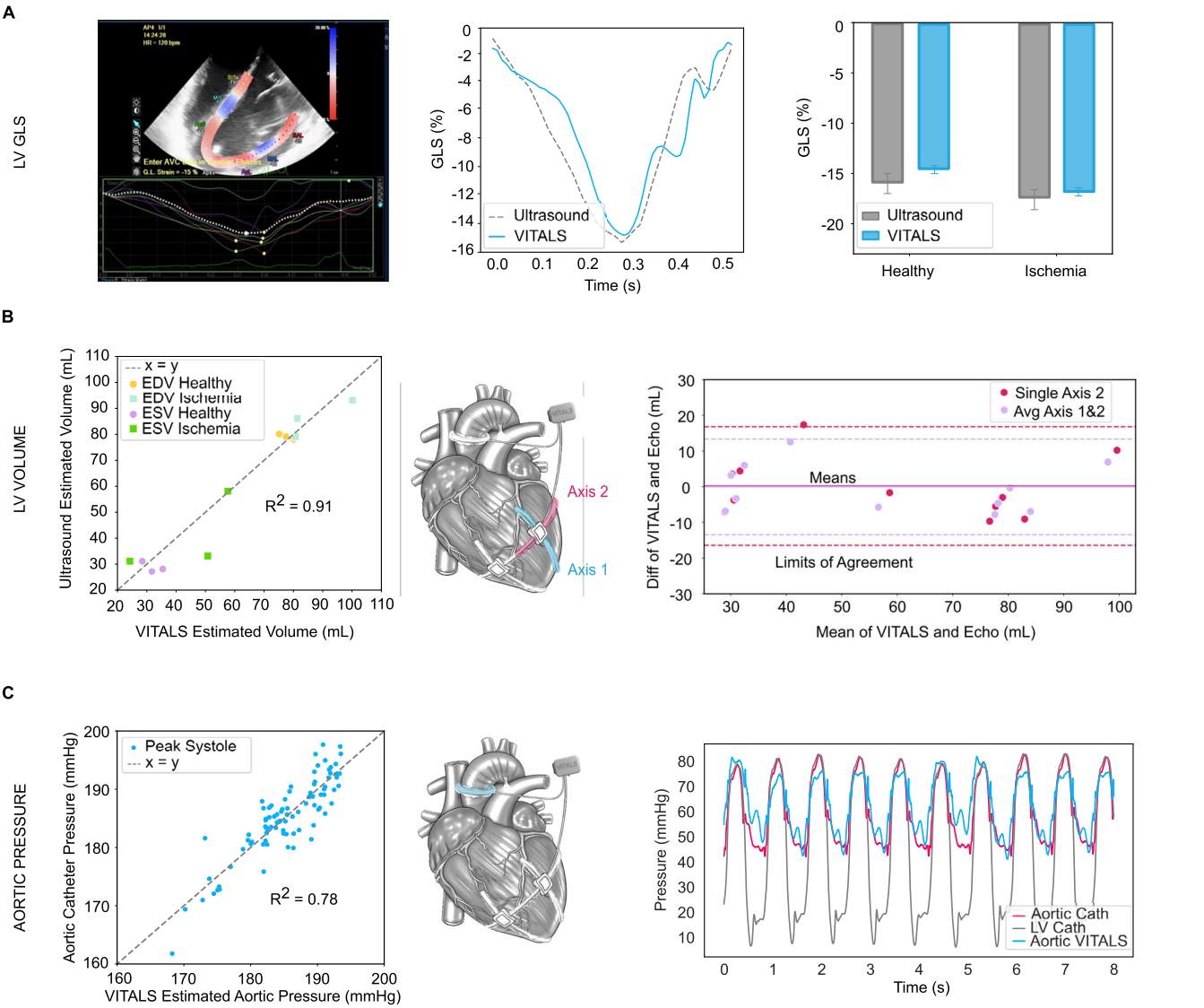


Fig. 4 | Correlation to clinical standard measurements. A Global Longitudinal Strain (GLS): (Left) A representative image of 2D strain derivation through speckle-tracking ultrasound (Middle) Ultrasound GLS compared to VITALS GLS (Right) A quantitative comparison of VITALS and ultrasound GLS in health and disease states (healthy p-value = 0.105, ischemia p-value = 0.46). **B** LV Volumes: (Left) End-diastolic volume and end-systolic volume (EDV and ESV) estimated by the LV-sensing hub in both healthy and disease states compared to ultrasound derived volumes (R^2 = 0.91) (Middle) Specification of LV sensing axes. (Right) A Bland-Altman plot of a single axis linearly calibrated to volume compared to the average of both axes. The mean of the single axis and the mean of the average of axes 2 and 1 is 0.04 mL and −0.01 mL, respectively. The single axis LOA is 16.8 mL, and the integration of the second axis reduces the LOA to 13.2 mL. **C** Aortic Pressure: (Left) VITALS-estimated peak systolic pressures following in-situ calibration compared with aortic catheter readings during epinephrine. (Middle) Illustration of aortic sensor location. (Right) Overlay of aortic sensor-estimated pressure on ground truth aortic and ventricular pressure tracings.

(measured by the sensor) and transmural strain (captured by ultrasound)[52]. This difference is well-documented in literature, with epicardial strain measurements showing particular sensitivity in detecting early myocardial dysfunction in conditions like concentric hypertrophy where endocardial-epicardial strain gradients may be altered[53]. Despite these inherent differences in measurement location, the correlation between VITALS and echocardiographic measurements supports the clinical relevance of an epicardial approach. VITALS measurements reveal distinct features during diastole, particularly the early and late diastolic strain rates. These features, well documented in high-resolution imaging studies, correspond to active myocardial relaxation and passive filling phases[54]. While conventional echocardiographic strain analysis may smooth these features due to post-processing, VITALS data undergo minimal processing, preserving these physiologically relevant signals.

Beyond strain, LV volume measurements offer additional insights into cardiac function, such as preload, ejection fraction, and stroke volume. Since absolute strain is preload-dependent, knowledge of end-diastolic dimension is crucial when interpreting strain measurements[55]. Previous studies have established a relationship between epicardial strain and LV volumes[30]. Using equation (1) (Methods), the sensor's strain values were transformed into LV volume, yielding a correlation with ultrasound-derived volumes (R^2 of 0.91, Fig. 4B). To assess the value of multiaxial sensing, an ablation study was performed comparing strain from the circumferential axis and the combined average of circumferential and longitudinal axes. The Bland-Altman plot (Fig. 4B) shows that the combined axis integration decreased the limit of agreement (LOA) by 20%, reducing variance in the measurements. Specifically, the LOA improved from 16.8 mL (circumferential axis alone) to 13.3 mL (combined axes), demonstrating the added robustness of integrating additional sensing axes.

The comprehensive evaluation of cardiac function extends beyond the analysis of myocardial strain and volume; the heart's ability to generate pressure and move blood through the circulation is a fundamental aspect of

its efficacy as a pump. Accurately measuring ventricular systolic pressure without contacting blood remains a challenge due to the difficulty of measuring generated tension in the myocardium. However, it is well-established that ventricular systolic pressure closely resembles aortic pressure during the ejection phase[56]. Because the aorta passively expands under LV-generated pressure, its circumferential strain can be used to estimate internal pressure[57,58]. A circumferential strain sensor was sutured around the aorta, providing a non-invasive means of measuring aortic pressure. The sensor was sutured at two locations (Supplementary Materials, Figure S5), informed by clinical guidance from the surgeons performing the procedure, to balance stability and surgical feasibility. While the accuracy of aortic strain measurements was not explicitly validated in this study, the primary focus was on capturing aortic pressure. A calibration process related MEMS pressure readings to aortic pressure. In this third porcine model ($n = 1$), pressure tracings from indwelling LV and aortic catheters were captured during dynamic afterload conditions induced by an epinephrine infusion. The aortic VITALS sensor tracked changes in peak systolic pressure, showing a linear correlation (R^2 of 0.78, Fig. 4C) with catheter-based measurements in this acute setting. The sensor readings were further compared against LV and aortic catheter data in steady, low-afterload conditions (Fig. 4C). The aortic pressure measurements shown in Fig. 4C (left) were obtained during a period of heightened pressure under epinephrine administration, with sensor calibration performed at this elevated state.The aortic pressure measurements shown in Fig. 4C (left) were obtained during a period of heightened pressure under epinephrine administration. The data for the measurements on the right was taken during a different phase of the experiment. Additionally, the correlation between VITALS-derived aortic pressure and LV pressure relies on the physiological relationship between ventricular and aortic pressures during ejection in the absence of outflow obstruction. This assumption, while valid in our experimental model, would need to be verified in clinical settings through routine echocardiographic assessment to account for potential development of aortic stenosis or other outflow tract abnormalities.

Detection of biventricular preload changes in real-time. Proactive management of postoperative HF patients necessitates a continuous and sensitive assessment of the hemodynamic state of the heart. Here, end-diastolic myocardial deformation is specifically examined as an indicator of preload, focusing on the mechanical stretch of the myocardial tissue rather than filling pressures. While this relationship between tissue stretch and filling pressure may vary with disease progression, particularly in conditions like HF with preserved ejection fraction (HFpEF) where ventricular compliance changes, tracking end-diastolic deformation provides valuable information about acute changes in ventricular filling[59]. Changes in preload can indicate severe postoperative complications, such as hypovolemic shock and vasoplegia, and acute right heart failure[60,61]. Indeed, preload management is a cornerstone of HF management, and the ability to detect response to therapies, such as diuretics, is critical for guideline-directed therapy. To showcase the sensitivity of VITALS to various hemodynamic conditions, variations in preload were simulated through inferior vena cava (IVC) occlusion, a technique designed to temporarily reduce venous return and mimic conditions of altered preload. The results, as depicted in Fig. 5A, illustrate VITALS' acute response to changes in preload affecting both the RV and LV. As a more intuitive representation of preload, or end-diastolic myocardial length, the VITALS signal is transformed from strain to change in length in millimeters, based on the initial calibration during fabrication. For further ease of interpretation, an aggregate change in length is determined by averaging measurements across both axes, with zero representing end-diastolic length prior to IVC occlusion. The observable downward shifts in peak values distinctly illustrate an immediate decrease in ventricular filling for both LV and RV, a clear indication of decreased preload, with a 9.8% decrease in filling dimension for the LV and 58% decrease in filling dimension for the RV. The more pronounced reduction in the RV is consistent with expectations given the RV's direct receipt of venous return and its relatively higher compliance compared to the LV[62].

Monitoring of biventricular functional deterioration. In addition to the detection of ventricular preload changes, the ability of a continuous monitoring solution to sensitively identify myocardial dysfunction in real time has the potential to enable a more proactive approach to post-operative HF management and interventional therapies. Ischemia is a major pathogenic mechanism underlying HF progression that drives myocardial dysfunction[63]. Acute postoperative ischemia is estimated to occur in 2–10% of cardiac surgery cases. It often occurs silently, as symptoms are difficult to distinguish between typical postoperative symptoms and masked by pain management therapies[64]. Given that ischemia-induced myocardial damage is irreversible, early detection and intervention are paramount[65]. To investigate VITALS' ability in this respect, an acute disease state was created by artificially occluding a coronary artery, as described above. After a seven-minute occlusion period, data collection commenced, capturing the immediate and subsequent responses of the heart to induced ischemia. The data represented in Fig. 5B and C reveals significant changes in both the LV and RV strain patterns post-MI, respectively. Notably, in the LV, an upward shift in the baseline end-diastolic length was observed, indicating an increase in preload and distension of the LV chamber. This response is recognized as a compensatory mechanism, wherein the heart attempts to maintain cardiac output amidst reduced function due to ischemia by invoking the Frank-Starling mechanism[66–68]. Furthermore, the data illustrates preferential dilation along one axis in the LV, specifically the axis that is more circumferential. This observation aligns with literature suggesting that the heart becomes more spherical in shape during ischemic HF conditions[67,69]. Additionally, the altered shape of the strain curve, characterized by a rounder peak indicative of "early systolic bulging" and "late systolic shortening," suggests a nuanced dynamic within the myocardium[70]. The initial expansion during early systole is thought to result from the lengthening of ischemic segments as they expand against increasing chamber pressure, a phenomenon previously demonstrated in sonomicrometry studies[71]. It is important to note that peak global longitudinal strain (GLS) increased immediately post-ligation, from an average of − 14.5% to − 16.8%; thus, this value alone does not communicate early dysfunction and suggests that highly accurate strain profiles may be necessary to fully capture the subtle mechanics indicative of dysfunction. The RV, although not directly subjected to infarction, also exhibited substantial dysfunction. This outcome could be attributed to the principle of interventricular dependence, where the RV's longitudinal shortening—and, by extension, its function—is heavily reliant on septal contribution[72]. The septum was likely impacted by LAD ligation[73,74]. The preferential impact observed on the VITALS axis that is more longitudinal in the RV further supports this theory, highlighting the interplay between right and left ventricular function and the systemic implications of localized ischemic events.

Following acute ischemia, ventricular fibrillation was induced with a second sustained ligation in the same location. Fibrillation is characterized by a highly-irregular, rapid cardiac contraction pattern. A Fourier analysis on the healthy and fibrillation VITALS GLS signals depicted in Fig. 5D, left, indicates a stark difference in the frequency makeup of these signals. Figure 5D, right, provides a spectrogram of the signal from the ischemic to fibrillation states over time, demonstrating a clear temporal indication of when the irregular beats begin.

Differentiation of inotropic states with integrated pressure monitoring. The integration of pressure and strain analysis is a powerful emerging tool that provides an understanding of myocardial work, offering insights into the heart's mechanical efficiency[75]. Information gained from assessing end-systolic dimension and pressure are particularly valuable, as they provide a global measure of ventricular elastance[76]. Ventricular elastance, a parameter describing the heart's inotropic or

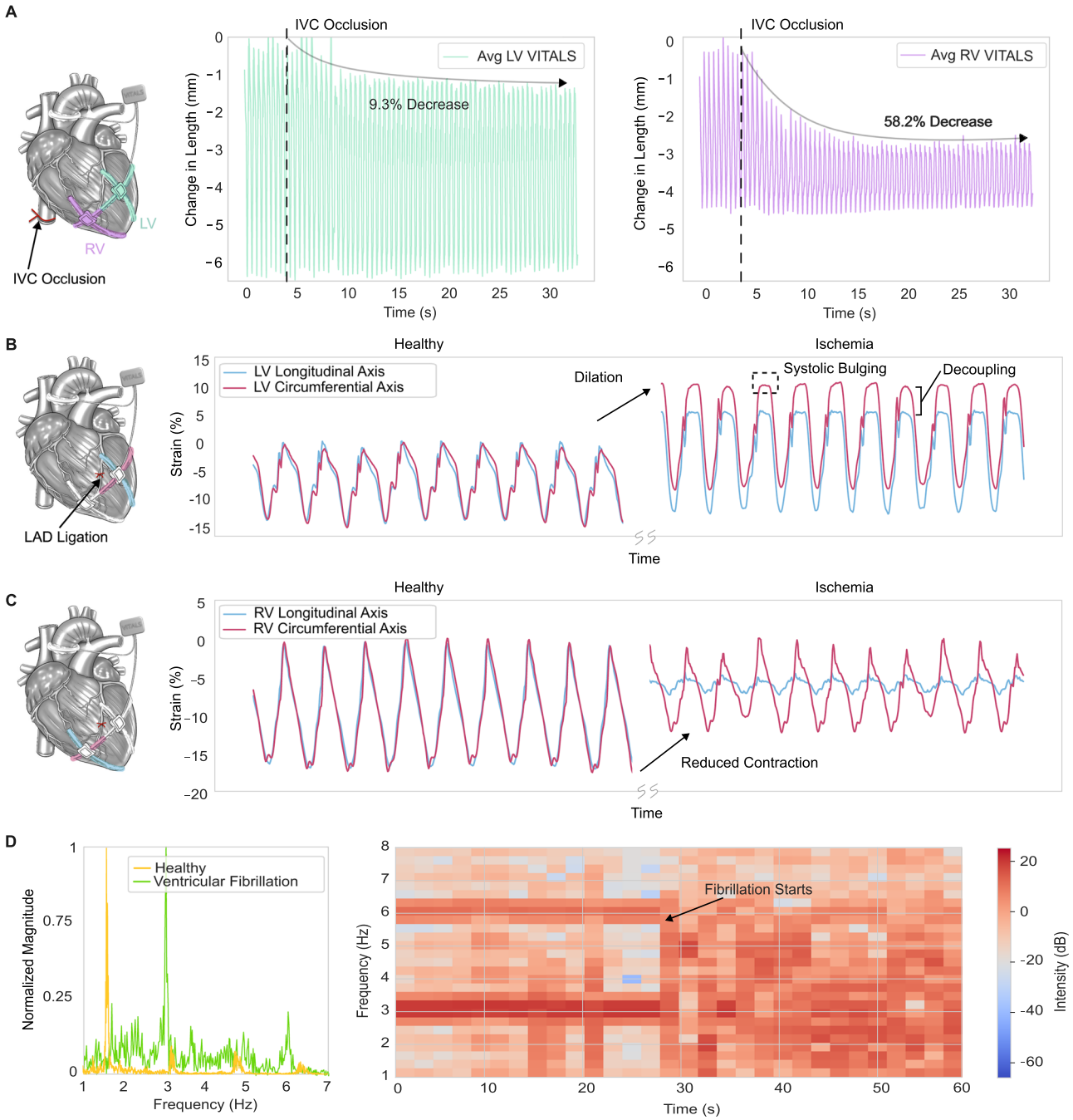


Fig. 5 | In vivo analysis of hemodynamic and functional changes. A LV (light green) and RV (light purple) sensor readings during IVC occlusion. The LV and RV sensor hubs show a 9.7% and 58% decrease in end-diastolic dimension, respectively. **B** LV sensor hub signals in the healthy and ischemic state. Heart rates are approximately 1.5 Hz and 3 Hz, respectively. During the ischemic state, there is global chamber dilation and a decoupling of the axes. Rounded diastolic peaks indicate systolic bulging. **C** RV sensor hub signals in the healthy and ischemic state. Both axes show decreased contraction, with a preferential decrease in the longitudinal axis. Heart rates are approximately 1.5 Hz and 3 Hz, respectively. **D** (Left) A frequency spectrum plot of LV sensor hub GLS during healthy (yellow) and fibrillation (green) states. (Right) Frequency characteristics of LV sensor hub GLS over time, showing when fibrillation starts.

contractile state, can be useful for evaluating pump function and the impact of therapeutic interventions on contractile status[77].

The ability to combine pressure and strain measurements is investigated over the course of increasing inotropy, induced by epinephrine administration. Figure 6A shows both VITALS GLS and aortic pressure over time, showing an increase in strain amplitude and peak pressure, respectively, as epinephrine takes effect. The complete response captures pressures reaching up to 175 mmHg during peak epinephrine effect. Elastance is typically investigated using an indwelling conductance catheter, which is used to record pressure-volume (PV) loops. Representative PV loops shown in Fig. 6B demonstrate the immediate effects of epinephrine, where the increase in ventricular elastance is evidenced by the leftward and upward shifting of the end-systolic point, indicating a higher stroke volume at an increased pressure. Comparatively, Fig. 6B plots VITALS estimated end-systolic pressure against the absolute value of end-systolic strain states. By drawing a line from the origin to these points, an end-systolic pressure-strain relationship emerges, providing similar information to the PV Loop's end-systolic pressure-volume relationship[78]. Notably, the curve generated under the influence of epinephrine exhibits a steeper slope compared to the pre-epinephrine baseline by a factor of 1.43, indicating an enhanced

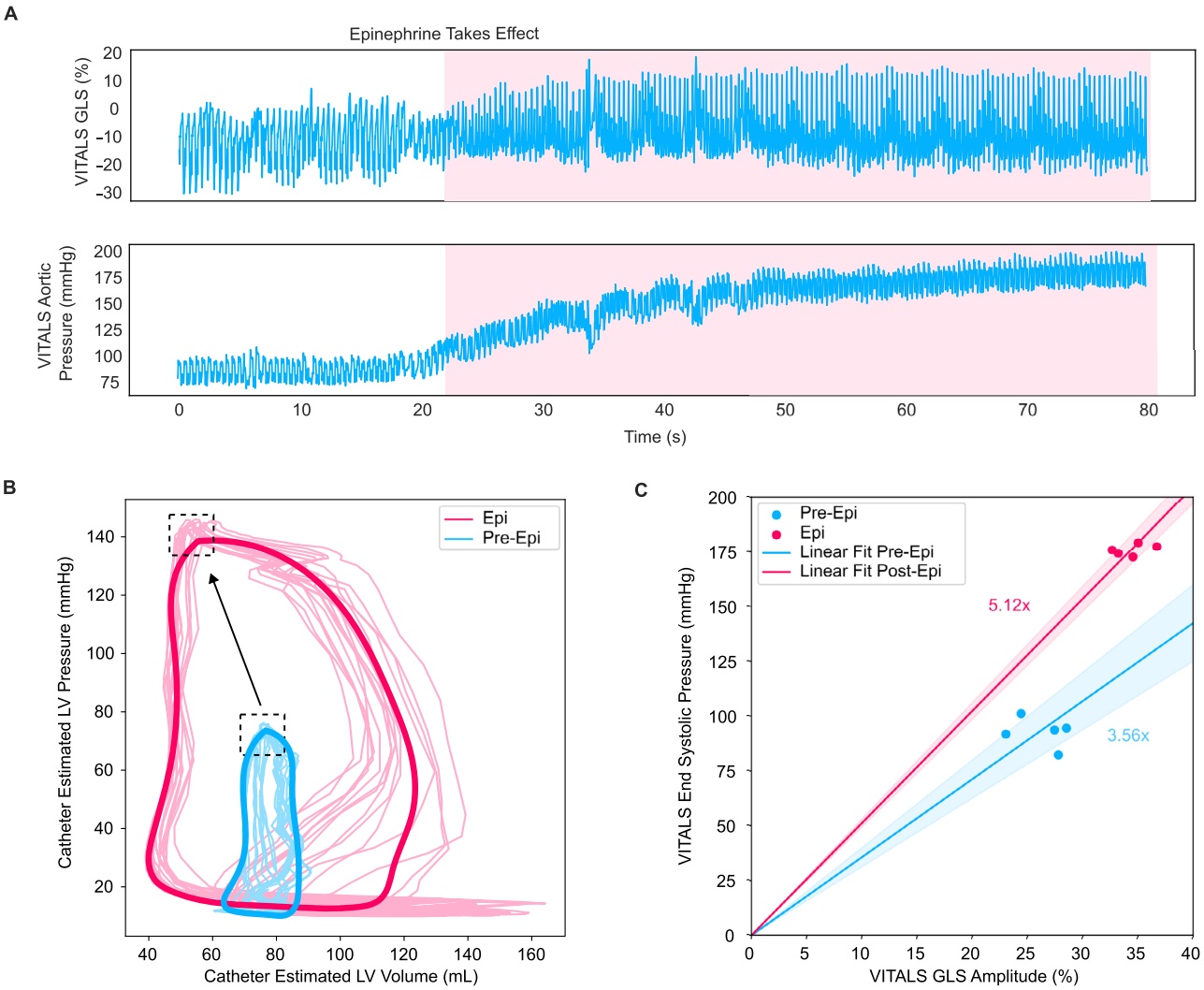


Fig. 6 | In vivo analysis of elastance. A (Top) VITALS LV GLS and (Bottom) VITALS aortic pressure over time after administration of epinephrine. **B** Pressure-volume loops derived from indwelling conductance catheters illustrating cardiac function before and after epinephrine. **C** VITALS generated end-systolic pressure strain curves, demonstrating its ability to differentiate between inotropic states.

contractile state of the heart. This finding in an acute, controlled setting demonstrates the potential of dual pressure-strain measurements to provide incremental insights into cardiac function and the impact of pharmacological agents.

Discussion

Heart failure (HF) remains a major global health issue, affecting millions and incurring significant healthcare costs. Despite advances in cardiac surgery, patients face a high risk of readmission or premature death after hospital discharge. Research has shown the substantial economic benefits of guideline-directed medical therapy for patients during the transition from hospital to home[79]. Innovations in implantable sensors have proven that continuous, highly accurate hemodynamic monitoring significantly reduces hospital readmissions and number of decompensation events compared to less sensitive measures, such as weight and activity logging[33,80]. Yet, unplanned readmissions and mortality rates persist, and there are currently limited approaches to soft strain sensing that meet the demanding requirements for continuous monitoring. To address this clinical gap, we evaluated the potential of continuous, multiaxial, and multistructural strain monitoring using implantable sensors through the VITALS prototype. This sensor network was developed as an initial prototype to explore potential use for implantation during open-heart surgeries, such as LVAD implantation, heart transplantation, and coronary artery bypass grafting (CABG) in patients with preoperative HF.

Building on previous work that introduced a durable, soft strain sensor[34], this research describes further enhancements by introducing a multimaterial encapsulation strategy, enabling multi-axial strain and pressure measurements, and validating the system in vivo under physiologically relevant conditions, demonstrating clinical applicability. The measurements demonstrated sensitivity to nuanced information about cardiac function across various hemodynamic states, including changes in preload and acute ischemic dysfunction. By integrating simultaneous aortic pressure measurements, additional insights were obtained, suggesting potential for differentiation between inotropic states. If validated in chronic settings, these measurements could enable comprehensive, continuous monitoring of patient status, facilitating the detection of critical changes in cardiac function and real-time tracking of the effects of pharmacological therapy in an ambulatory setting. This approach could potentially establish a data-driven feedback loop for physician care, potentially helping to address the cycle of HF.

Several limitations of the current work should be considered. Importantly, this study was conducted in a small number of animals in an open-chest model. While sufficient to demonstrate initial feasibility, future preclinical studies in large animal models should include larger sample sizes and a broader range of disease states to more robustly establish correlations

with clinical gold standards, evaluate the effects of closed-chest conditions on sensor readings and accuracy in the presence of fibrotic encapsulation, and assess the clinical relevance across diverse HF etiologies, including HFpEF. As the system is intended for ambulatory use, variations in body position that may affect pressure readings must also be considered. Additionally, the sensor hub's calibration for LV chamber volume and aortic valve measurements may need periodic recalibration to account for cardiac remodeling and aortic stenosis, respectively. Employing pulse wave velocity techniques using dual aortic sensors could provide real-time adjustments to aortic stiffness changes over time[31,81]. Further, the current embodiment of the sensor is limited to epicardial measurements on the free walls of both the LV and RV, excluding direct measurements of endocardial strain or the septal wall, which are typically captured using traditional ultrasound methods. Nonetheless, valuable insights can still be obtained from the VITALS system. Notably, epicardial strain has been shown to be significantly altered during cardiac dysfunction, providing an important indicator of cardiac health[82–84]. Additionally, measurements from the LV free wall can signal early septal activation, suggesting that interpretations from the free wall alone may provide sufficient diagnostic value even in the absence of direct septal measurements[85]. To fully harness this capability, the integration of electrodes to track the heart's electrical signaling for precise timing analysis would be necessary. Future engineering iterations and studies to evaluate these hypotheses will be critical areas of continued development and a subject of future work.

While beyond the proof-of-concept scope of this study, the VITALS system is designed to facilitate future engineering developments that enable durable, chronic deployment. Further engineering efforts to optimize the system for chronic in vivo conditions would include waterproofing the electronics to prevent fluid ingress. This could be achieved by applying a coating layer on top of the circuitry before silicone casting, such as the biocompatible urethane-epoxy blend provided by Master Bond®(Master Bond®, USA). The system's long-term durability should then also be investigated to evaluate its resilience under cyclic loading in realistic conditions and ensure consistent signal fidelity. While no mechanical degradation was observed in benchtop testing, long-term biocompatibility and signal drift remain potential concerns under chronic, impanted use and must be explored further in large animal models before clinical translation. Another engineering consideration is the integration of wireless communication methods. The sensor technology demonstrated by the VITALS prototype is inherently compatible with future wireless implementation. Given that the sensing electronics employ standard industrial MEMS capacitors, wireless communication can feasibly utilize established methodologies, such as employing a passive LC resonator design with the MEMS acting as a variable capacitor, similar to approaches used in CardioMEMS (Abbott, USA)[86,87]. The primary challenge in this regard will be efficiently reading multiple sensors, a challenge that could be addressed using an approach similar to that proposed by Wang et al.[88] that leverages multiple sensor-specific resonant frequencies. Alternatively, this technology could leverage rechargeable batteries and Bluetooth modules, similar to those utilized in contemporary implantable cardiac defibrillators (ICDs) (Entrant, Abbott, and Aurora EV-ICD, Medtronic).

Although this technology is proposed for initial use in patients already receiving open-heart surgery, the ultimate goal would be to expand its utility to implantation through a minimally invasive procedure. This concept could be implemented by adopting an approach similar to the LARIAT device that uses a minimally invasive procedure to obtain percutaneous epicardial access for left atrial appendage ligation (SentreHEART, Inc, Redwood City, CA) or using a minimally invasive subxiphoid approach and fluoroscopic guidance, used in the implantation of the extravascular ICD from Medtronic[89,90]. Fixation to the heart could be addressed using an adhesive hydrogel coating on the bottom of the sensor, eliminating the need for precise suturing and ensuring further stability of the epicardial and aortic sensors under ambulatory conditions. Such coatings have been shown to suppress fibrosis, providing added benefits[91,92].

Successful clinical integration will hinge on how well these continuous measurements can influence treatment decisions in a standardized, actionable way. For the initial proposed clinical use cases of this technology, strain and preload-guided interventions are on their way to being established, and this transition could be more fully facilitated by such a high-fidelity, continuous measurement system. For example, GLS is being investigated as an early indicator of antibody-mediated rejection in heart transplantation, and progressive dilation of the RV after LVAD implantation can suggest proactive support to prevent RV failure[93,94]. With the rise of artificial intelligence and machine learning in healthcare, the rich data provided by these sensors could be leveraged to tailor interventions and enhance patient care.

Ultimately, VITALS shows promise for improving HF management by providing a continuous, real-time view of cardiac function. Initial results suggest that its ability to capture critical cardiac data continuously could potentially close significant gaps in HF treatment, though substantial additional validation would be required before clinical implementation.

Methods

Sensor fabrication

VITALS employs a network of MEMS barometers; the BMP384 package from Bosch was selected for this application. The PCB layout was designed using Altium and manufactuterd on a 0.1 mm thick flexible substrate (JLCPCB). To prevent delamination and assist in folding, a 0.2 mm polyimide stiffener was added to the back of each MEMS device. A TCA9548A multiplexer from Texas Instruments communicated with each of the sensors using the I2C protocol and in turn communicated with a single Arduino Due microcontroller (Arduino, USA) for data collection. Data from the sensors was read using a custom MATLAB interface for real-time processing and visualization. The silicone elements were cast onto the PCB using 3D printed molds (Formlabs Inc., USA) according to methods in[34] using Ecoflex™ 00-10 (Smooth On Inc, USA). A secondary mold was used to encapsulate the VITALS elements in the Ecoflex™ Gel 000-35. To calibrate the sensors, a VITALS hub was secured to a 3D printed jig, and each sensing element was dynamically stretched by a maximum of 5 mm using a muscle-lever (300C Dual Mode Muscle Lever, Aurora Scientific) at 1.5 Hz. The calibration yielded an affine fit between MEMS barometer signal in Pascal to sensor strain (or change in length). A depiction of this setup and calibration can be found in Supplementary Materials, Supplementary Fig. 1.

Benchtop studies

Using a 3D-printed prolate spheroidal mold (Stratasys Ltd., USA) a ventricular phantom was cast with Ecoflex™ 00-30, chosen to closely mimic the diastolic mechanical properties of heart tissue. To simulate heart inflation, the phantom was manually inflated with air. Single VITALS elements were prepared by using Ecoflex™ 00-10 as the sensing substrate. Subsequently, a second layer of 0.75 mm thickness was added to the bottom; the control case had Ecoflex™ 00-10 for this layer, while the other utilized Ecoflex™ 000-35 to explore the utility of shear strain dissipation in maintaining signal fidelity under various conditions. Sensors were then securely attached to the exterior of the phantom by bonding their distal ends, ensuring stable positioning during manual inflation. To simulate fibrosis, a discrete section on each sensor, 10 mm distal to the PCB, was bonded to the phantom using cyanoacrylate, creating shear loading conditions. The signal from each sensor was normalized against maximum strain, which was measured manually using a flexible ruler. This setup allowed for the detailed observation of non-axial loading conditions on signal fidelity.

In vivo porcine studies

All procedures involving animals were conducted with the protocol approval of Stanford University's Institutional Animal Care and Use Committee (IACUC), specifically its Administrative Panel on Laboratory Animal Care (APLAC) (#34477). The study was conducted in compliance with the regulations set forth by the APLAC office and was carried out in a humane manner, limiting pain and distress for the acute surgical cases. The

study involved three Sus Scrofa Yorkshire strain pigs, each weighing between 60-80 kilograms and requisitioned from the same supplier. All pigs underwent similar anesthetic regimens tailored to their specific weights. All pigs were intubated and placed on a ventilator; maintained by Isoflurane through inhalation. Vascular access was achieved using ear vein catheterization for fluid delivery. An 18-22-gauge cannula was inserted in the femoral artery percutaneously for direct blood pressure monitoring and arterial blood sampling throughout the operation. A similar cannula was inserted through the femoral vein to obtain central venous pressure monitoring and mixed venous blood samples. Blood pressure was supported with the use of epinephrine and fluid support such as normal saline and 5–10% dextrose. The pigs' temperatures were maintained by thermal support. Vital parameters such as ECG, BP, ETCO2, %SpO2, %FiO2, and temperature were monitored throughout the surgical procedure.

After a balanced anesthetic regimen was achieved, median sternotomy was performed, exposing the heart and the great vessels. The pericardium was accessed using electrocautery; pericardial stay sutures were placed using 2-0 silk sutures and snapped to the drape for retraction and increasing operational space. There was no cardiopulmonary bypass used for any of the procedures. The sensors were attached to the apex of the heart using 5-0 Prolene suture, and the silicone limbs of the sensors were secured to each ventricle (see Fig. 1B for a depiction of sensor network placement). Transonic pressure transducer catheters were placed in the pulmonary artery, aortic root and right ventricle for continuous monitoring of pressure. The sensors were placed in appreciation of the anatomy, avoiding impeding any coronary arteries. AD Instrument Ventri-Cath 507S PV Loop Straight catheter was placed in the left ventricle trans-apically for continuous pressure-volume monitoring. As per the protocol, ultrasound echocardiography was utilized at multiple time points throughout each case for measuring left ventricle volume, tracking changes in ventricular strain, and achieving calibration of the PV loop catheter. Upon completion of the experiments, animals were humanely euthanized through the use of pentobarbital, as approved by the protocol.

For the first experiment, a single sensor element was placed on the epicardium and sutured at two points, putting the sensor under slight tension. Black nylon fabric, cut into 2mm squares, was sutured onto the left ventricular (LV) epicardium along the sensor's length, aligned with the longitudinal axis. Two smartphones, set to record at 60 fps, were mounted above the chest to ensure a clear view, using phone holders attached to the overhead surgical light. A calibration jig with known three-dimensional coordinates was briefly placed in view for spatial reference, then removed. MATLAB imaging software, DLTdv8, was used to reconstruct 3D points and subsequently fit with a spline, and strain was defined as the change in length of this spline[48]. Camera and sensor signals were synchronized through a brief tapping on the sensor, creating a visible and detectable signal spike in the video and sensor data. The sensor signal was correlated to the measured strain. Two points on a rigid object within the video frame were tracked to create a baseline, and the change in distance between these 3D points was used to calculate error.

For the second experiment, a sensor network comprised of an LV hub and RV hub was implanted, with one sensor on the LV and another on the RV, positioned longitudinally and circumferentially, respectively. Inferior vena cava (IVC) banding using a gortex band was performed for 30 seconds, during which signals were recorded. Following a return to steady-state hemodynamics, left anterior descending (LAD) artery ligation was performed. Echocardiographic transepicardial 4-chamber view images were taken before (healthy) and after (ischemic condition) the procedure, with three single-beat videos captured at each stage. Fibrillation was induced following the acute ischemic state with re-ligation of the LAD. The ligation was held until ventricular fibrillation was noted on the electrocardiogram.

For the final experiment, a sensor network was deployed, including an additional element wrapped around the aorta. Sensor signals were recorded continuously. An intravenous (IV) administration of 20 mcg of epinephrine was performed, with sensor data tracked throughout the epinephrine's effect, noting increased pressures and heart rates. The aortic sensor was calibrated for measuring aortic pressure using methods described in Magkoutas et al.[31].

Echocardiography and sensor comparison

Echocardiographic images were acquired by a trained echocardiographer using a Philips iE33 ultrasound machine, equipped with an S5-1 probe. This equipment was chosen for its advanced imaging capabilities and reliability in cardiac imaging studies. LV volumes were determined through a two-step process. Initially, manual tracing of the LV boundaries was performed on the captured images to outline the ventricular area. Subsequently, the automated Simpson's method was applied to these tracings to calculate the LV volumes. For the assessment of myocardial strain, the semi-automated Cardiac Motion Quantification (CMQ) post-processing feature of the Philips iE33 machine was utilized. This feature provides speckle-tracking derived strain for 6 segments of the LV. The reported global longitudinal strain is an average of all 6 segments, and this average was used for comparison to the LV Sensor hub longitudinal axis signal. To ensure accurate comparisons between echocardiographic measurements and sensor data, image acquisition was manually synchronized with the recordings from the sensors. To account for the slight time discrepancy between echo readings and sensor recordings, the first five cardiac cycles were extracted and averaged from the sensor dataset to yield values for the six healthy and disease states. To transform LV sensor hub measurements to volume for comparison, existing established analytical relationships between directional strain and chamber volume were used[95]:

$$\Delta V = kC_0^2 L_0 (1 - C_S)^2 (1 - L_S) \quad (1)$$

Where C_0 and L_0 are end-diastolic lengths of axis 2 and axis 1 at implantation, respectively, and and C_S and L_S are peak axis 2 and axis 1 strains, respectively. To calculate change in volume we have:

$$V = V_0 - kC_0^2 L_0 (1 - C_S)^2 (1 - L_S) \quad (2)$$

This practical approach allows for calibration to be established at the time of implantation, where a single end-systolic volume (ESV) and end-diastolic volume (EDV) measurement can define the constants V_0 and k. Importantly, C_0 and L_0 are constants which can also be aggregated into a single coefficient accounted for during calibration.

Statistics

Statistical analyses for both benchtop and in vivo comparisons were conducted using a two-tailed Student's t-test. The significance level for all statistical tests was set at $p = 0.05$, and p-value less than 0.05 was considered indicative of a statistically significant difference between the compared groups.

Data availability

No datasets were generated or analysed during the current study.

Received: 16 October 2024; Accepted: 9 March 2025;
Published online: 03 May 2025

References

1. Urbich, M. et al. A systematic review of medical costs associated with heart failure in the usa (2014–2020). *Pharmacoeconomics* **38**, 1219–1236 (2020).
2. Ong, M. K. et al. Effectiveness of remote patient monitoring after discharge of hospitalized patients with heart failure: the better effectiveness after transition–heart failure (beat-hf) randomized clinical trial. *JAMA Int. Med.* **176**, 310–318 (2016).
3. Takeda, K. et al. Incidence and clinical significance of late right heart failure during continuous-flow left ventricular assist device support. *J. Heart Lung Transplant.* **34**, 1024–1032 (2015).

4. Dalen, M., Lund, L. H., Ivert, T., Holzmann, M. J. & Sartipy, U. Survival after coronary artery bypass grafting in patients with preoperative heart failure and preserved vs reduced ejection fraction. *JAMA Cardiol.* **1**, 530–538 (2016).
5. Jezovnik, M. K. et al. Medical complications in patients with lvad devices. *Eur. Soc. Cardiol.* **14**, 37 (2017).
6. Krittanawong, C. et al. Integration of novel monitoring devices with machine learning technology for scalable cardiovascular management. *Nat. Rev. Cardiol.* **18**, 75–91 (2021).
7. Emmons-Bell, S., Johnson, C. & Roth, G. Prevalence, incidence and survival of heart failure: a systematic review. *Heart* **108**, 1351–1360 (2022).
8. Ammar, K. A. et al. Prevalence and prognostic significance of heart failure stages: application of the american college of cardiology/ american heart association heart failure staging criteria in the community. *Circulation* **115**, 1563–1570 (2007).
9. Dharmarajan, K. et al. Diagnoses and timing of 30-day readmissions after hospitalization for heart failure, acute myocardial infarction, or pneumonia. *Jama* **309**, 355–363 (2013).
10. De Couto, G., Ouzounian, M. & Liu, P. P. Early detection of myocardial dysfunction and heart failure. *Nat. Rev. Cardiol.* **7**, 334–344 (2010).
11. Mann, D. L. & Bristow, M. R. Mechanisms and models in heart failure: the biomechanical model and beyond. *Circulation* **111**, 2837–2849 (2005).
12. Mann, D. L. & Felker, G. M. Mechanisms and models in heart failure: a translational approach. *Circulation Res.* **128**, 1435–1450 (2021).
13. Chun, S. et al. Lifetime analysis of hospitalizations and survival of patients newly admitted with heart failure. *Circulation: Heart Fail.* **5**, 414–421 (2012).
14. Kemp, C. D. & Conte, J. V. The pathophysiology of heart failure. *Cardiovascular Pathol.* **21**, 365–371 (2012).
15. Metra, M. et al. Worsening of chronic heart failure: Definition, epidemiology, management and prevention. a clinical consensus statement by the heart failure association of the european society of cardiology. *Eur. J. Heart Fail.* **25**, 776–791 (2023).
16. Jong, P., Yusuf, S., Rousseau, M. F., Ahn, S. A. & Bangdiwala, S. I. Effect of enalapril on 12-year survival and life expectancy in patients with left ventricular systolic dysfunction: a follow-up study. *Lancet* **361**, 1843–1848 (2003).
17. Busse, L. W., Barker, N. & Petersen, C. Vasoplegic syndrome following cardiothoracic surgery—review of pathophysiology and update of treatment options. *Crit. Care* **24**, 1–11 (2020).
18. Cha, M.-J., Kim, H.-S., Kim, S. H., Park, J.-H. & Cho, G.-Y. Prognostic power of global 2d strain according to left ventricular ejection fraction in patients with st elevation myocardial infarction. *PloS one* **12**, e0174160 (2017).
19. Ochs, A. et al. Myocardial mechanics in dilated cardiomyopathy: prognostic value of left ventricular torsion and strain. *J. Cardiovascular Magn. Reson.* **23**, 136 (2021).
20. Reindl, M. et al. Prognostic implications of global longitudinal strain by feature-tracking cardiac magnetic resonance in st-elevation myocardial infarction. *Circulation: Cardiovascular Imaging* **12**, e009404 (2019).
21. Zheng, Y. et al. Morphological, functional, and biomechanical progression of lv remodelling in a porcine model of hfpef. *J. Biomech.* **144**, 111348 (2022).
22. Xu, R. et al. Identification of early cardiac dysfunction and heterogeneity after pressure and volume overload in mice by high-frequency echocardiographic strain imaging. *Front. Cardiovascular Med.* **9**, 1071249 (2023).
23. Edvardsen, T., Helle-Valle, T. & Smiseth, O. A. Systolic dysfunction in heart failure with normal ejection fraction: speckle-tracking echocardiography. *Prog. cardiovascular Dis.* **49**, 207–214 (2006).
24. Cameli, M. et al. Left atrial longitudinal strain by speckle tracking echocardiography correlates well with left ventricular filling pressures in patients with heart failure. *Cardiovascular ultrasound* **8**, 1–9 (2010).
25. Marwick, T. H., Shah, S. J. & Thomas, J. D. Myocardial strain in the assessment of patients with heart failure: a review. *JAMA Cardiol.* **4**, 287–294 (2019).
26. Motoki, H. et al. Incremental prognostic value of assessing left ventricular myocardial mechanics in patients with chronic systolic heart failure. *J. Am. Coll. Cardiol.* **60**, 2074–2081 (2012).
27. Katz, A. M. & Rolett, E. L. Heart failure: when form fails to follow function. *Eur. heart J.* **37**, 449–454 (2016).
28. Kovács, A., Lakatos, B., Tokodi, M. & Merkely, B. Right ventricular mechanical pattern in health and disease: beyond longitudinal shortening. *Heart Fail. Rev.* **24**, 511–520 (2019).
29. Skaarup, K. G. et al. Link between myocardial deformation phenotyping using longitudinal and circumferential strain and risk of incident heart failure and cardiovascular death. *European Heart Journal-Cardiovascular Imaging* jead075 (2023).
30. Dual, S. A. et al. Continuous heart volume monitoring by fully implantable soft strain sensor. *Adv. Healthc. Mater.* **9**, 2000855 (2020).
31. Magkoutas, K. et al. Continuous monitoring of blood pressure and vascular hemodynamic properties with miniature extravascular hall-based magnetic sensor. *Basic Transl. Sci.* **8**, 546–564 (2023).
32. Rajiah, P. S. et al. Myocardial strain evaluation with cardiovascular mri: physics, principles, and clinical applications. *RadioGraphics* **42**, 968–990 (2022).
33. Stevenson, L. W., Ross, H. J., Rathman, L. D. & Boehmer, J. P. Remote monitoring for heart failure management at home. *J. Am. Coll. Cardiol.* **81**, 2272–2291 (2023).
34. Kight, A. et al. Decoupling transmission and transduction for improved durability of highly stretchable, soft strain sensing: Applications in human health monitoring. *Sensors* **23**, 1955 (2023).
35. Yogev, D. et al. Current state of the art and future directions for implantable sensors in medical technology: Clinical needs and engineering challenges. *APL bioengineering***7** (2023).
36. Cong, P., Young, D. J., Hoit, B. & Ko, W. H. Novel long-term implantable blood pressure monitoring system with reduced baseline drift. In *2006 International Conference of the IEEE Engineering in Medicine and Biology Society*, 1854–1857 (IEEE, 2006).
37. Boland, C. S. Quantifying the contributing factors toward signal fatigue in nanocomposite strain sensors. *ACS Appl. Polym. Mater.* **2**, 3474–3480 (2020).
38. Harea, E., Datta, S., Stěnička, M. & Stoček, R. Undesirable aspects of fatigue on stretchable elastomer sensors. In *Nanoscience and Nanotechnology in Security and Protection against CBRN Threats*, 95–105 (Springer, 2020).
39. Cahn, G., Pierron, O. & Antoniou, A. Electrical performance evolution and fatigue mechanisms of silver-filled polymer ink under uniaxial cyclic stretch. *Flex. Print. Electron.* **6**, 035008 (2021).
40. Huneau, B. et al. Fatigue crack initiation in a carbon black–filled natural rubber. *Rubber Chem. Technol.* **89**, 126–141 (2016).
41. Llerena Zambrano, B. et al. Soft electronics based on stretchable and conductive nanocomposites for biomedical applications. *Adv. Healthc. Mater.* **10**, 2001397 (2021).
42. Xu, L. et al. 3d multifunctional integumentary membranes for spatiotemporal cardiac measurements and stimulation across the entire epicardium. *Nat. Commun.* **5**, 3329 (2014).
43. Qiu, X., Yin, H. & Xing, Q. Research progress on fatigue life of rubber materials. *Polymers* **14**, 4592 (2022).
44. Shangguan, W.-B. et al. Experiment and modeling of uniaxial tension fatigue performances for filled natural rubbers. *Mater. Des.* **58**, 65–73 (2014).

45. Cadwell, S. M., Merrill, R., Sloman, C. & Yost, F. Dynamic fatigue life of rubber. *Rubber Chem. Technol.* **13**, 304–315 (1940).
46. Mendez, K. L. et al. Smartsleeve: A sutureless, soft robotic epicardial device that enables switchable on-off drug delivery in response to epicardial ecg sensing. *Device* (2024).
47. Pirozzi, I. et al. Rvex: Right ventricular external device for biomimetic support and monitoring of the right heart. *Adv. Mater. Technol.* **7**, 2101472 (2022).
48. Hedrick, T. L. Software techniques for two-and three-dimensional kinematic measurements of biological and biomimetic systems. *Bioinspiration Biomim.* **3**, 034001 (2008).
49. Stendahl, J. C. et al. Multiaxial pressure-strain analysis of regional myocardial work in the setting of graded coronary stenoses and dobutamine stress. *Am. J. Physiol.-Heart Circulatory Physiol.* **325**, H492–H509 (2023).
50. Ruhhammer, J. et al. Arterial strain measurement by implantable capacitive sensor without vessel constriction. In *2012 Annual International Conference of the IEEE Engineering in Medicine and Biology Society*, 535–538 (IEEE, 2012).
51. Munz, M. R., Faria, M. A., Monteiro, J. R., Águas, A. P. & Amorim, M. J. Surgical porcine myocardial infarction model through permanent coronary occlusion. *Comp. Med.* **61**, 445–452 (2011).
52. Nagata, Y., Wu, V. C.-C., Otsuji, Y. & Takeuchi, M. Normal range of myocardial layer-specific strain using two-dimensional speckle tracking echocardiography. *PLoS One* **12**, e0180584 (2017).
53. Xu, L. et al. Layer-specific strain in patients with heart failure using cardiovascular magnetic resonance: not all layers are the same. *J. Cardiovascular Magn. Reson.* **22**, 81 (2020).
54. Wei, L. et al. Peak early diastolic strain rate improves prediction of adverse cardiovascular outcomes in patients with st-elevation myocardial infarction. *La radiologia Med.* **128**, 1372–1385 (2023).
55. Nobre De Matos Pereira Vieira, M. et al. 3077 load dependency of left ventricular longitudinal strain by 2d-speckle tracking echocardiography: myth or reality? *Eur. Heart J.* **40**, ehz745–0033 (2019).
56. Swamy, G., Kuiper, J., Gudur, M. S., Olivier, N. B. & Mukkamala, R. Continuous left ventricular ejection fraction monitoring by aortic pressure waveform analysis. *Ann. Biomed. Eng.* **37**, 1055–1068 (2009).
57. Greenfield Jr, J. C. & Patel, D. J. Relation between pressure and diameter in the ascending aorta of man. *Circulation Res.* **10**, 778–781 (1962).
58. Barnett, G., Mallos, A. & Shapiro, A. Relationship of aortic pressure and diameter in the dog. *J. Appl. Physiol.* **16**, 545–548 (1961).
59. Schwinger, R. et al. The failing human heart is unable to use the frank-starling mechanism. *Circulation Res.* **74**, 959–969 (1994).
60. Shaefi, S. et al. Vasoplegia after cardiovascular procedures—pathophysiology and targeted therapy. *J. Cardiothorac. Vasc. anesthesia* **32**, 1013–1022 (2018).
61. Ende, J., Wilbring, M., Ende, G. & Koch, T. The diagnosis and treatment of postoperative right heart failure. *Dtsch. Ärzteblatt Int.* **119**, 514 (2022).
62. Axell, R. G., Hoole, S. P., Hampton-Till, J. & White, P. A. Rv diastolic dysfunction: time to re-evaluate its importance in heart failure. *Heart Fail. Rev.* **20**, 363–373 (2015).
63. Pagliaro, B. R., Cannata, F., Stefanini, G. G. & Bolognese, L. Myocardial ischemia and coronary disease in heart failure. *Heart Fail. Rev.* **25**, 53–65 (2020).
64. Nicolas, J. et al. Myocardial infarction after cardiac surgery: when to intervene? *J. Thorac. Cardiovascular Surg.* **165**, 1195–1201 (2023).
65. Saku, K., Yokota, S., Nishikawa, T. & Kinugawa, K. Interventional heart failure therapy: A new concept fighting against heart failure. *J. Cardiol.* **80**, 101–109 (2022).
66. Del Buono, M. G. et al. Heart failure after st-elevation myocardial infarction: beyond left ventricular adverse remodeling. *Current Problems in Cardiology* 101215 (2022).
67. Cohn, J. N., Ferrari, R., Sharpe, N. & an International Forum on Cardiac Remodeling. Cardiac remodeling—concepts and clinical implications: a consensus paper from an international forum on cardiac remodeling. *J. Am. Coll. Cardiol.* **35**, 569–582 (2000).
68. Calvieri, C. et al. Left ventricular adverse remodeling in ischemic heart disease: Emerging cardiac magnetic resonance imaging biomarkers. *J. Clin. Med.* **12**, 334 (2023).
69. Abidov, A. et al. Transient ischemic dilation ratio of the left ventricle is a significant predictor of future cardiac events in patients with otherwise normal myocardial perfusion spect. *J. Am. Coll. Cardiol.* **42**, 1818–1825 (2003).
70. Brainin, P. Myocardial postsystolic shortening and early systolic lengthening: current status and future directions. *Diagnostics* **11**, 1428 (2021).
71. Lyseggen, E. et al. A novel echocardiographic marker of end systole in the ischemic left ventricle: "tug of war" sign. *Am. J. Physiol.-Heart Circulatory Physiol.* **296**, H645–H654 (2009).
72. Voelkel, N. F. et al. Right ventricular function and failure: report of a national heart, lung, and blood institute working group on cellular and molecular mechanisms of right heart failure. *Circulation* **114**, 1883–1891 (2006).
73. Jones, B. M. et al. Ventricular septal rupture complicating acute myocardial infarction: a contemporary review. *Eur. heart J.* **35**, 2060–2068 (2014).
74. Triposkiadis, F. et al. The interventricular septum: structure, function, dysfunction, and diseases. *J. Clin. Med.* **11**, 3227 (2022).
75. Cauwenberghs, N. et al. Area of the pressure-strain loop during ejection as non-invasive index of left ventricular performance: a population study. *Cardiovascular ultrasound* **17**, 1–11 (2019).
76. Kaseda, S., Tomoike, H., Ogata, I. & Nakamura, M. End-systolic pressure-length relations during changes in regional contractile state. *Am. J. Physiol.-Heart Circulatory Physiol.* **247**, H768–H774 (1984).
77. Chen, C.-H. et al. Noninvasive single-beat determination of left ventricular end-systolic elastance in humans. *J. Am. Coll. Cardiol.* **38**, 2028–2034 (2001).
78. Faragli, A. et al. Cardiovascular magnetic resonance-derived left ventricular mechanics—strain, cardiac power and end-systolic elastance under various inotropic states in swine. *J. Cardiovascular Magn. Reson.* **22**, 79 (2020).
79. Wei, C., Heidenreich, P. A. & Sandhu, A. T. The economics of heart failure care. *Progress in Cardiovascular Diseases* (2024).
80. Fraiche, A. M., Eapen, Z. J. & McClellan, M. B. Moving beyond the walls of the clinic: opportunities and challenges to the future of telehealth in heart failure. *JACC: Heart Fail.* **5**, 297–304 (2017).
81. Sutton-Tyrrell, K. et al. Elevated aortic pulse wave velocity, a marker of arterial stiffness, predicts cardiovascular events in well-functioning older adults. *Circulation* **111**, 3384–3390 (2005).
82. Howard-Quijano, K. et al. Left ventricular endocardial and epicardial strain changes with apical myocardial ischemia in an open-chest porcine model. *Physiological Rep.* **4**, e13042 (2016).
83. Lin, J. et al. Comparison of myocardial layer-specific strain and global myocardial work efficiency during treadmill exercise stress in detecting significant coronary artery disease. *Front. Cardiovascular Med.* **8**, 786943 (2022).
84. Ancedy, Y. et al. Does layer-specific strain using speckle tracking echocardiography improve the assessment of left ventricular myocardial deformation? a review. *Arch. cardiovascular Dis.* **113**, 721–735 (2020).
85. Galli, E. et al. The saga of dyssynchrony imaging: Are we getting to the point. *Front. Cardiovascular Med.* **10**, 1111538 (2023).

86. Abraham, W. T. et al. Wireless pulmonary artery haemodynamic monitoring in chronic heart failure: a randomised controlled trial. *Lancet* **377**, 658–666 (2011).
87. Fonseca, M. A., English, J. M., Von Arx, M. & Allen, M. G. Wireless micromachined ceramic pressure sensor for high-temperature applications. *J. microelectromechanical Syst.* **11**, 337–343 (2002).
88. Wang, B., Long, J. & Teo, K. H. Multi-channel capacitive sensor arrays. *Sensors* **16**, 150 (2016).
89. Srivastava, M. C., See, V. Y., Dawood, M. Y. & Price, M. J. A review of the lariat device: insights from the cumulative clinical experience. *Springerplus* **4**, 1–13 (2015).
90. Thompson, A. E. et al. The development of the extravascular defibrillator with substernal lead placement: A new frontier for device-based treatment of sudden cardiac arrest. *J. cardiovascular Electrophysiol.* **33**, 1085–1095 (2022).
91. Liu, J. et al. Intrinsically stretchable electrode array enabled in vivo electrophysiological mapping of atrial fibrillation at cellular resolution. *Proc. Natl Acad. Sci.* **117**, 14769–14778 (2020).
92. Wu, J. et al. Adhesive anti-fibrotic interfaces on diverse organs. *Nature* 1–8 (2024).
93. Otto, M. E. B. et al. Acute cellular rejection in heart transplant patients: Insights of global longitudinal strain, myocardial work, and an exclusive group of chagas disease. *Front. Cardiovascular Med.* **9**, 841698 (2022).
94. Wang, T. S., Cevasco, M., Birati, E. Y. & Mazurek, J. A. Predicting, recognizing, and treating right heart failure in patients undergoing durable lvad therapy. *J. Clin. Med.* **11**, 2984 (2022).
95. Samuel, T. J. et al. Integration of longitudinal and circumferential strain predicts volumetric change across the cardiac cycle and differentiates patients along the heart failure continuum. *J. Cardiovascular Magn. Reson.* **25**, 55 (2023).
96. Boutry, C. M. et al. A stretchable and biodegradable strain and pressure sensor for orthopaedic application. *Nat. Electron.* **1**, 314–321 (2018).
97. Zhang, Q. et al. A stretchable strain sensor system for wireless measurement of musculoskeletal soft tissue strains. *Adv. Mater. Technol.* **8**, 2202041 (2023).
98. Zhang, L. M. et al. Self-healing, adhesive, and highly stretchable ionogel as a strain sensor for extremely large deformation. *Small* **15**, 1804651 (2019).
99. Chen, R. et al. Highly stretchable and fatigue resistant hydrogels with low young's modulus as transparent and flexible strain sensors. *J. Mater. Chem. C.* **6**, 11193–11201 (2018).
100. Choi, D. Y. et al. Highly stretchable, hysteresis-free ionic liquid-based strain sensor for precise human motion monitoring. *ACS Appl. Mater. interfaces* **9**, 1770–1780 (2017).
101. Zhang, H., Lowe, A., Kalra, A. & Yu, Y. A flexible strain sensor based on embedded ionic liquid. *Sensors* **21**, 5760 (2021).
102. Ren, J. et al. A graphene rheostat for highly durable and stretchable strain sensor. *InfoMat* **1**, 396–406 (2019).
103. Emig, R. et al. Passive myocardial mechanical properties: meaning, measurement, models. *Biophys. Rev.* 1–24 (2021).

Acknowledgements

The authors would like to thank Dr. Murat Fudim (Duke), Dr. Inchang Hwang (SNU), and Dr. Ileana Pirozzi for their valuable insights on the experiments and data visualization.

Author contributions

A.K. was responsible for the overall leadership of the project, encompassing its design, execution, analysis, and manuscript preparation. M.H., M.S., Y.O., and G.I. assisted in designing and executing animal experiments. S.T. contributed to the engineering and design of the prototypes. A.S. and Y.P. were involved in data collection and manuscript editing. F.S. contributed to experimental preparation, data collection, and data analysis. AH, MM, KR, and DM contributed to data interpretation, visualisation, and editing. S.D. and M.C. contributed to the project's overall conceptualization, substantial manuscript preparation, and advising.

Competing interests

A patent application has been filed through Stanford University's Office of Licensing and Technology, application number 63/443421 filed 2/5/2023 and current pending status, with the United States Patent and Trademark Office. A.K., M.C., D.M., S.D., and A.M. are named inventors. The authors report no other competing interests.

Additional information

Supplementary information The online version contains supplementary material available at https://doi.org/10.1038/s44385-025-00017-x.

Correspondence and requests for materials should be addressed to Ali Kight.

Reprints and permissions information is available at http://www.nature.com/reprints

Publisher's note Springer Nature remains neutral with regard to jurisdictional claims in published maps and institutional affiliations.

Open Access This article is licensed under a Creative Commons Attribution-NonCommercial-NoDerivatives 4.0 International License, which permits any non-commercial use, sharing, distribution and reproduction in any medium or format, as long as you give appropriate credit to the original author(s) and the source, provide a link to the Creative Commons licence, and indicate if you modified the licensed material. You do not have permission under this licence to share adapted material derived from this article or parts of it. The images or other third party material in this article are included in the article's Creative Commons licence, unless indicated otherwise in a credit line to the material. If material is not included in the article's Creative Commons licence and your intended use is not permitted by statutory regulation or exceeds the permitted use, you will need to obtain permission directly from the copyright holder. To view a copy of this licence, visit http://creativecommons.org/licenses/by-nc-nd/4.0/.

© The Author(s) 2025